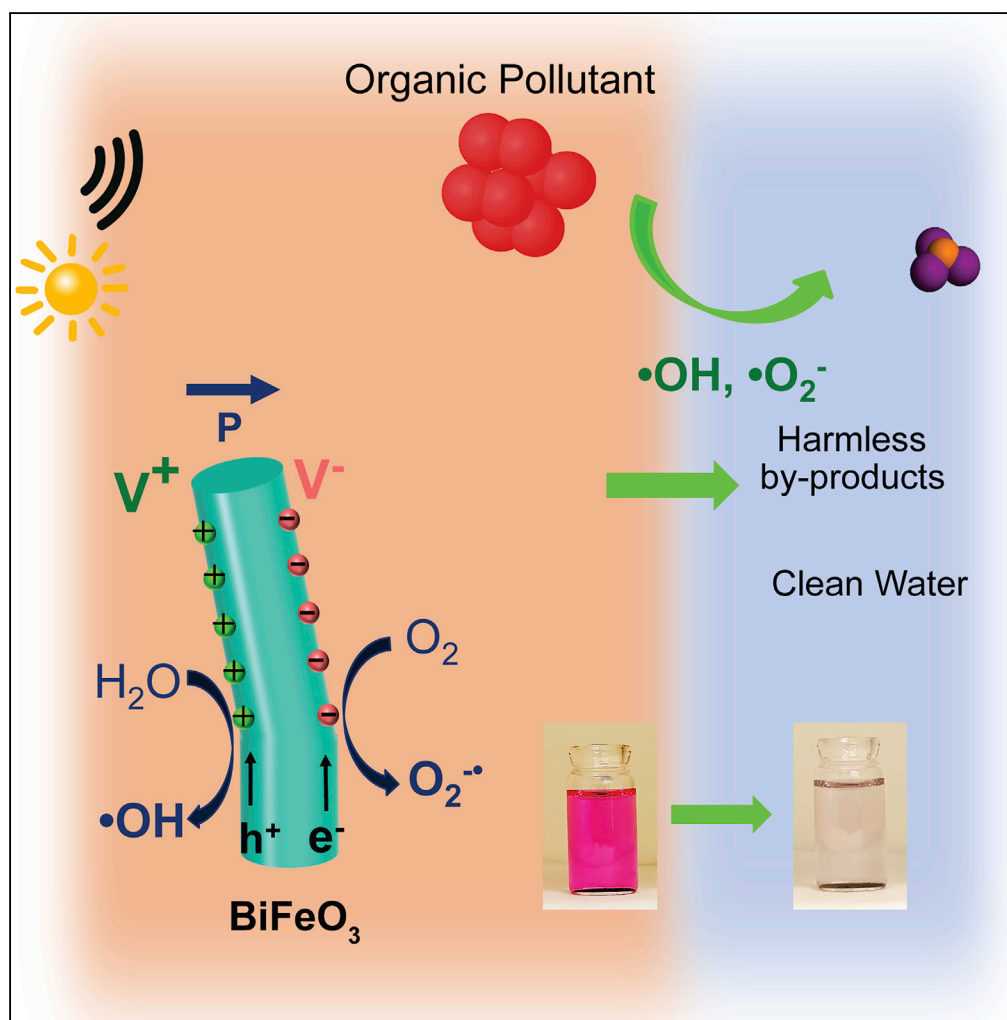Article

Piezoelectrically Enhanced Photocatalysis with BiFeO₃ Nanostructures for Efficient Water Remediation

Fajer Mushtaq,
Xiangzhong Chen,
Marcus Hoop, ...,
Chiara Gattinoni,
Bradley J. Nelson,
Salvador Pané

fmushtaq@ethz.ch (F.M.)
chenxian@ethz.ch (X.C.)

HIGHLIGHTS
Use of photocatalytic and ferroelectric BiFeO₃ nanosheets and nanowires

Harnessing solar energy and mechanical vibrations for organic pollutant removal

Elevated performance under mechanical stress was attributed to the piezotronic effect

Hydroxyl radicals and holes were dominant species for degradation of organics

Article

Piezoelectrically Enhanced Photocatalysis with BiFeO₃ Nanostructures for Efficient Water Remediation

Fajer Mushtaq,[1,*] Xiangzhong Chen,[1,6,*] Marcus Hoop,[1] Harun Torlakcik,[1] Eva Pellicer,[2] Jordi Sort,[3,4] Chiara Gattinoni,[5] Bradley J. Nelson,[1] and Salvador Pané[1]

SUMMARY

Designing new catalysts that can efficiently utilize multiple energy sources can contribute to solving the current challenges of environmental remediation and increasing energy demands. In this work, we fabricated single-crystalline BiFeO₃ (BFO) nanosheets and nanowires that can successfully harness visible light and mechanical vibrations and utilize them for degradation of organic pollutants. Under visible light both BFO nanostructures displayed a relatively slow reaction rate. However, under piezocatalysis both nanosheets and nanowires exhibited higher reaction rates in comparison with photocatalytic degradation. When both solar light and mechanical vibrations were used simultaneously, the reaction rates were elevated even further, with the BFO nanowires degrading 97% of RhB dye within 1 hr (k-value 0.058 min^{-1}). The enhanced degradation under mechanical vibrations can be attributed to the promotion of charge separation caused by the internal piezoelectric field of BFO. BFO nanowires also exhibited good reusability and versatility toward degrading four different organic pollutants.

INTRODUCTION

Environmental pollution and shortage of clean energy are among the most pressing problems that threaten sustainable development of human civilization. Water pollution caused by discharge of toxic, synthetic dyes into effluents is one of the major sources of environmental pollution (Matilainen et al., 2010). The presence of even trace amounts of these synthetic dyes in water is extremely harmful because of their carcinogenic and mutagenic nature (de Lima et al., 2007; Umbuzeiro et al., 2005; Ekici et al., 2001; Chung, 1983). Owing to their high solubility and chemical stability, most of these synthetic dyes easily escape conventional water treatment methods and persist in the environment (Fracasso et al., 1992). Advanced oxidation process (AOP) is a cost-effective and green approach to degrade such toxic dyes into harmless products, such as CO_2 and H_2O, using highly reactive species, including hydroxyl and superoxide radicals (Julkapli et al., 2014; Dong et al., 2007).

Photocatalysis is one of the most extensively researched fields of AOP, in which a semiconductor with a suitable bandgap can efficiently absorb light and form photogenerated electron-hole pairs. These electrons and holes can then migrate to the surface of the photocatalyst and initiate the oxidative/reductive processes, resulting in degradation of organic pollutants (Yan et al., 2013). One of the main drawbacks that limits practical use of photocatalysts is the high electron-hole recombination rate, which ultimately lowers their photocatalytic efficiency. To overcome this problem, wide bandgap semiconductors, such as titanium dioxide (TiO_2), are extensively used. However, having a wide bandgap limits the light absorption of these materials to the UV region (Núñez et al., 2017). Hence, researchers have proposed new strategies, including developing novel nanostructures, using co-catalysts (Pt, Pd, and RuO_2), doping with rare-earth or transition metals, and fabricating heterojunctions to tune the bandgap of these materials, to lower the electron-hole recombination rate, and to increase the lifetime of the charge carriers (Long and Prezhdo, 2015; Sakthivel et al., 2004; Mushtaq et al., 2015, 2016; Zhang et al., 2011). Although such approaches can improve the separation of photogenerated electrons and holes, they rely heavily on the use of expensive catalysts such as noble metals and suffer from complicated fabrication processes, which, in turn, create obstacles to their practical application (Wang et al., 2016).

Apart from chemically modifying the wide bandgap, physical methods such as the application of external electric fields to an electrochemical cell were also employed to separate the electron-hole pairs and,

[1]Multi-Scale Robotics Lab (MSRL), Institute of Robotics and Intelligent Systems (IRIS), ETH Zurich, CH-8092 Zurich, Switzerland

[2]Departament de Física, Facultat de Ciències, Universitat Autònoma de Barcelona, Campus UAB, E-08193 Bellaterra (Cerdanyola del Vallès), Spain

[3]Institució Catalana de Recerca i Estudis Avançats (ICREA), Passeig Lluís Companys 23, E-08010 Barcelona, Spain

[4]Departament de Física, Universitat Autònoma de Barcelona, E-08193 Bellaterra (Cerdanyola del Vallès), Spain

[5]Materials Theory, ETH Zurich, CH-8093 Zurich, Switzerland

[6]Lead Contact

*Correspondence:
fmushtaq@ethz.ch (F.M.),
chenxian@ethz.ch (X.C.)

https://doi.org/10.1016/j.isci.2018.06.003

hence, improve their photocatalytic performance (Barroso et al., 2013; Pesci et al., 2013). Even though this method has demonstrated strong potential to increase the photocatalytic efficiency, its high cost, complicated device structure, and difficult operation conditions provide significant challenges for practical use (Li et al., 2014; Hong et al., 2016; Wang et al., 2016).

Generating a localized electric field directly on a photocatalyst's surface is a more practical approach than applying a macroscale electric field in a chemical cell because of cost and lower energy consumption. Combining piezoelectric materials with visible light photocatalysts is one way to achieve this. Piezoelectric materials can generate an internal electric field under strain and, hence, induce separation of photogenerated electric charges (Xue et al., 2015; Hong et al., 2010; Singh and Khare, 2017; Yun et al., 2018; Nan et al., 2017). This approach was used to fabricate primarily core-shell nanostructures, in which the core was composed of piezoelectric materials, such as ZnO, BaTiO$_3$, and NaNbO$_3$, whereas the shell consisted of visible light photocatalysts, including CuS, FeS, and AgO$_2$. In this approach, it was possible to achieve enhanced reaction efficiency by using the dual stimuli of light and mechanical vibrations (Hong et al., 2016; Xiao et al., 2016; Li et al., 2015; Jia et al., 2018). However, fabrication of such dual-phase core-shell nanomaterials raises further complications, such as complex synthesis and weak mechanical coupling between the piezoelectric and photocatalytic counterparts under strain for extended periods of time.

Low bandgap (i.e., visible light photocatalytic properties) and piezoelectric properties can co-exist in a single material. The use of BiFeO$_3$ (BFO) as a promising candidate for visible light photocatalysis has been demonstrated owing to its low bandgap of ~2.1 eV (Xian et al., 2011; Soltani and Entezari, 2013; Mocherla et al., 2013). In addition, BFO also possesses good piezo/ferroelectric performance with a large spontaneous polarization in excess of 100 μC cm^{-2} and piezoelectric coefficient (d_{33}) of about 100 pm/V (Singh et al., 2006; Jung Min et al., 2012). We assume these properties render BFO an excellent candidate for efficiently using both light and vibrational energy for catalytic degradation of organic pollutants, without the need for coupling it to other materials or using an external bias (Qi et al., 2018).

In this work, we fabricated pure, single-crystalline BFO nanosheets (NSs) and nanowires (NWs), which are both visible light photoactive and piezoelectric. These BFO nanostructures were able to harness photonic as well as mechanical energy for the degradation of model organic pollutants such as rhodamine B (RhB). By coupling their photocatalytic and piezoelectric properties, degradation of RhB dye was greatly enhanced. Reactive species trapping experiments revealed the underlying mechanism of their catalytic performance. Development of these nanostructures contributes to the use of green technologies, such as harnessing natural sunlight and scavenging waste energies, such as noise and vibrations, for efficient environmental applications.

RESULTS AND DISCUSSION

BFO NSs and NWs were fabricated by a hydrothermal synthesis approach by carefully tuning growth conditions, including surface chemistry, temperature, and duration of the reaction. The fabrication scheme of BFO NSs and NWs is presented in Figure 1A. First, concentrated ammonia was added to a solution of bismuth and iron salts to achieve co-precipitation of Bi^{3+} and Fe^{3+} ions (Li et al., 2012; Sun et al., 2014). Then a mineralizer (5 M NaOH) was added to the solution. The mixture was then sealed in an autoclave and placed in an oven at elevated temperature for hydrothermal treatment. Hydrothermal synthesis uses the dissolution-crystallization mechanism. Under hydrothermal conditions, the precipitates reacted with NaOH to dissolve and form complex ions. This was followed by the formation of BFO crystals in the supersaturated region by nucleation, precipitation, dehydration, and growth of these complex ions over time (Xu et al., 2016). For BFO NSs, the reaction temperature was 140°C and the reaction time was 72 hr. BFO NWs were fabricated by a surfactant-assisted hydrothermal route at 180°C for 72 hr. In this approach, the soft-templating effect of polyethylene glycol (PEG) was employed to direct the growth of BFO crystals to form BFO NWs (Harraz, 2008; Song et al., 2014). BFO NS fabricated in this study are rhombic with an edge length of 2–3 μm and a thickness of about 150 nm (Figure 1B). The BFO NWs are about 30 μm long, with an average diameter between 200 and 700 nm (Figure 1C).

The crystalline structure of the BFO NSs and NWs were analyzed using X-ray diffraction (XRD) and transmission electron microscopy (TEM). XRD investigation performed on BFO nanostructures (Figure 2A) showed that for both NS and NW structures all peaks can be assigned to the pure phase of BiFeO$_3$ (JCPDS No. 82–1254), indicating a rhombohedral perovskite structure with the space group *R3c*. Further evaluation
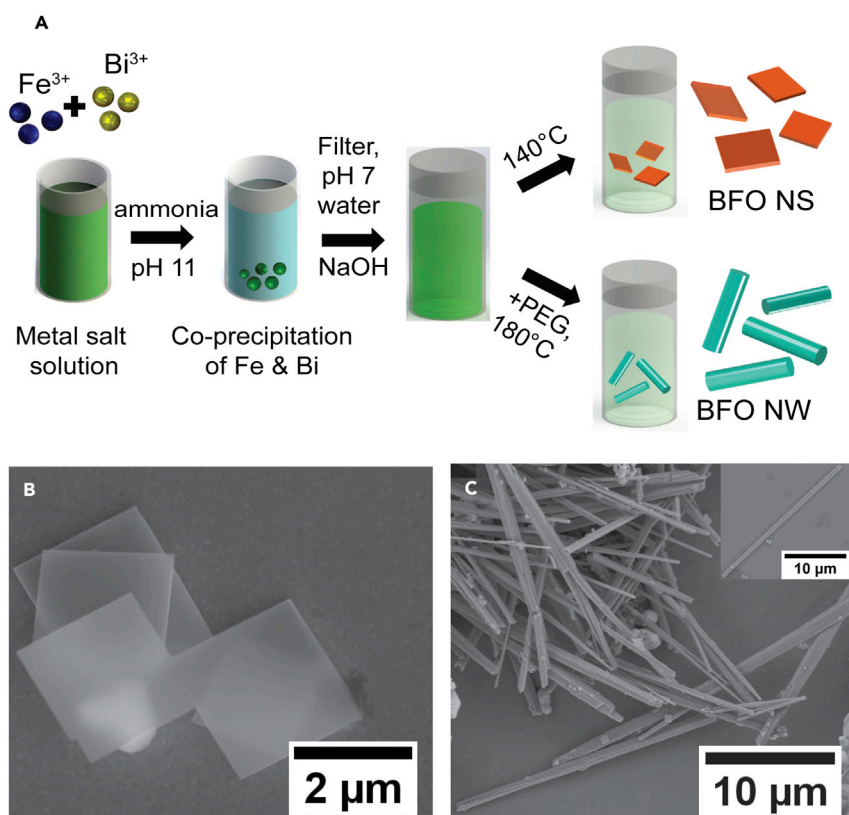
Figure 1. Fabrication Scheme and Morphology of BFO NSs and NWs

(A) Scheme showing how to fabricate BFO NSs and NWs using hydrothermal synthesis.

(B) Scanning electron microscope image showing overlapped BFO NSs.

(C) Scanning electron microscope image showing several BFO NWs. In the inset a single NW is shown.

of the BFO NS sample shows that the NSs have an average coherent diffraction length of 137 $\pm$ 10 nm and cell parameters $a = b = 5.58567 \pm 0.00002$ Å and $c = 13.88767 \pm 0.00005$ Å. A similar analysis performed on a BFO NW sample shows an average coherent diffraction length of 117 $\pm$ 10 nm and cell parameters $a = b = 5.58599 \pm 0.00003$ Å and $c = 13.88635 \pm 0.00004$ Å. TEM analysis of the BFO NS sample shows the presence of well-defined NS (Figure 2B), in agreement with scanning electron microscopy observations. A high-resolution TEM (HRTEM) image of a single NS is presented in Figure 2C and features an intact and orderly structure. The inset is the corresponding selected area electron diffraction (SAED) pattern, which confirms the single-crystalline structure. The spots in the SAED pattern have been indexed according to the *R3c* structure, and the result is compatible with a [024] growth direction of the NS. This is in agreement with the observed texture in the XRD pattern (Figure 2A) and in line with other reports from the literature on BFO NSs (Yang et al., 2014). The TEM image obtained for the BFO NW sample shows that the as-prepared nanopowder consists of straight NWs with a tip-like ending, suggesting a [006] growth direction (Figure 2D). Its corresponding HRTEM image corroborates the presence of an intact, orderly, single-crystalline structure. The planes with interplanar d-spacings of 0.28 nm and 0.19 nm match the (104) and (024) crystal faces, respectively (Figure 2E). The inset presents the corresponding SAED pattern, showing the single crystalline nature of BFO NW and further confirming the growth along the [006] direction (also see Figure S2).

The light absorption properties of BFO NS and NW samples were investigated using UV-visible diffuse reflectance spectra (DRS) at room temperature. From Figure 3A, we can observe that both BFO nanostructures exhibit strong absorption in the UV and visible light region. Careful observation reveals that in comparison with the BFO NWs, the BFO NSs display a higher absorbance in the visible light region. The bandgaps of BFO NSs and NWs were calculated using the Kubelka-Munc function ($[\alpha h\upsilon]^2$ vs photon energy [$h\upsilon$]) for the direct bandgap semiconductor (Figure 3B). The bandgaps were estimated to be 2.075 eV for BFO NSs and 2.1 eV for BFO NWs, which are consistent with the literature (Soltani and Entezari, 2013; Xian et al.,
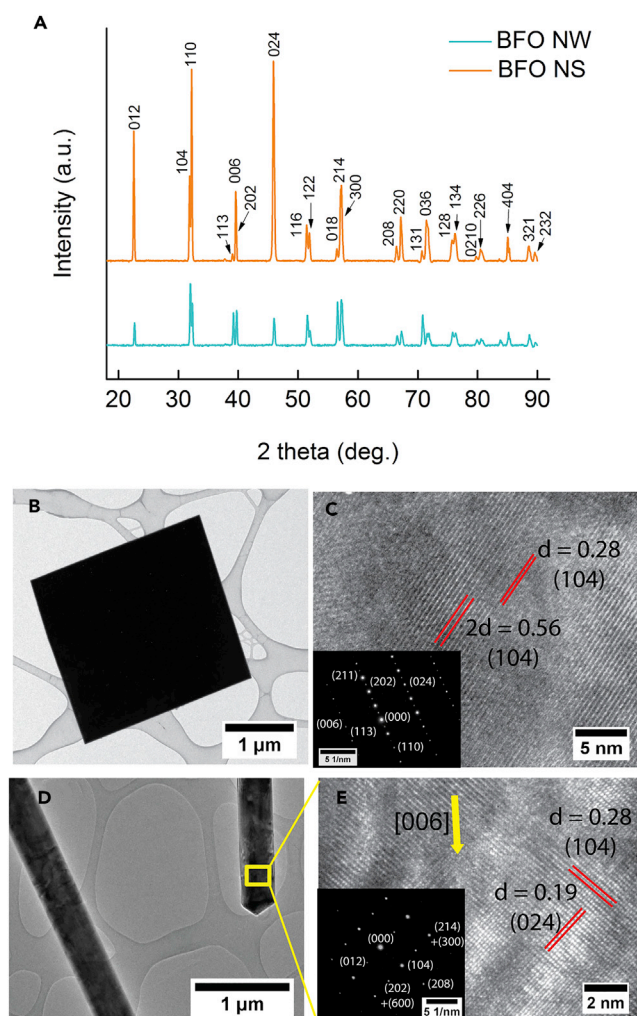
Figure 2. Structural Characterization of BFO NS and NW Samples

(A) XRD patterns obtained for BFO NSs and NWs.

(B) TEM image showing a single BFO NS.

(C) The corresponding HRTEM image. Its electron diffraction pattern is shown in the inset.

(D) TEM image showing two BFO NWs.

(E) HRTEM image obtained from the marked area in Figure 2D, showing the growth direction of the NW along the [006] direction. The inset shows its electron diffraction pattern.

2011). These small bandgap values for BFO NSs and NWs indicate that they can be used as photocatalysts under visible light.

The piezoelectricity of a single BFO NW was directly probed using piezoresponse force microscopy (PFM). A conductive cantilever tip was used in contact mode to apply an alternating voltage to the sample and induce piezoelectric surface oscillations. These oscillations were sensed through the consequent cantilever deflection. Figure 3 presents the PFM phase (C) and amplitude (E) images for BFO NWs. From the PFM phase images, a clear phase contrast between different regions of the NW can be observed. These regions with different contrast represent the domains with opposite out-of-plane polarization orientations. The amplitude image (Figure 3E) also shows the presence of distinct and randomly distributed ferroelectric domains. To further investigate the ferroelectric nature of our BFO samples, local piezoresponse hysteresis loops were obtained by sweeping the applied DC bias while simultaneously measuring the phase and amplitude response. The excitation voltage waveform was a stepwise increasing pulsed DC voltage, superimposed on a small AC voltage. To minimize the possible interference caused by electrostatic forces, the
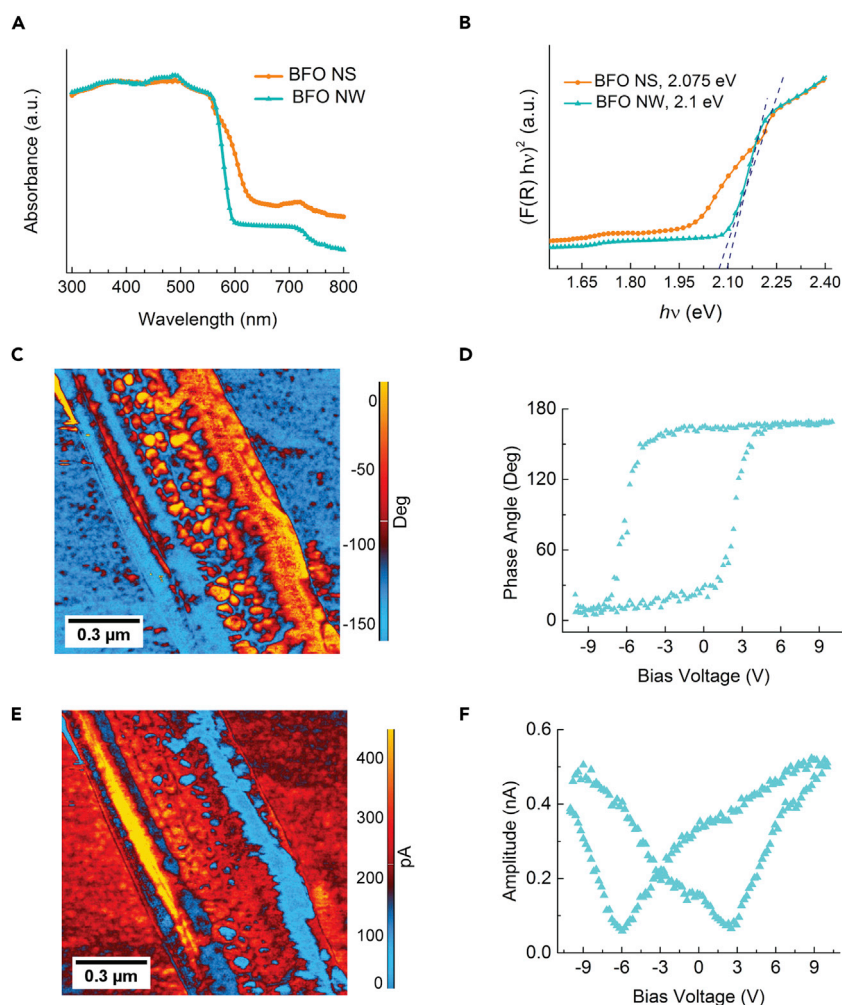
Figure 3. Optical and Piezoelectric Characterization of BFO Nanostructures
(A) UV-Vis DRS spectra obtained for BFO NS and NW samples.
(B) The corresponding Kubelka-Munc plot.
(C and D) PFM characterization of BFO NW showing the phase response.
(E and F) PFM characterization of BFO NW showing the amplitude response.

AC response signal was acquired only during the off-phase of the voltage pulse sequence (Chen et al., 2013). From the phase loop presented in Figure 3D it can be clearly observed that the polarization can be switched to the opposite direction by sweeping the tip bias. The average phase contrast is close to 180°, confirming that the measured signal originates from the electromechanical response rather than from electrostatic forces (Chen et al., 2017; Avinash et al., 2011). The amplitude of the response signal in PFM is directly related to the local strain of the BFO nanostructures (Figure 3F). This amplitude versus bias voltage curve is also hysteretic, and its shape resembles a butterfly loop, which is a well-established characteristic of ferroelectric materials (Xie et al., 2008). The piezoresponse phase and amplitude loops for BFO NWs are horizontally shifted. This asymmetry in the loops can be attributed to many factors, including the imprint effect, internal bias fields inside the materials, and/or a work function difference between the top Pt-coated Si probe and the bottom gold electrode (Chen et al., 2016). The well-defined piezoresponse hysteresis loops confirm the ferroelectric nature of our BFO NW samples. For NSs, similar analysis was performed and is presented in Figure S3.

The ability of BFO nanostructures to degrade RhB using light and mechanical vibrations was investigated. Both BFO samples gradually degrade RhB dye under UV-visible light over 3 hr (66% for NS and 60% for NW samples). In contrast, the control sample without BFO displayed a negligible response (Figure 4A). The
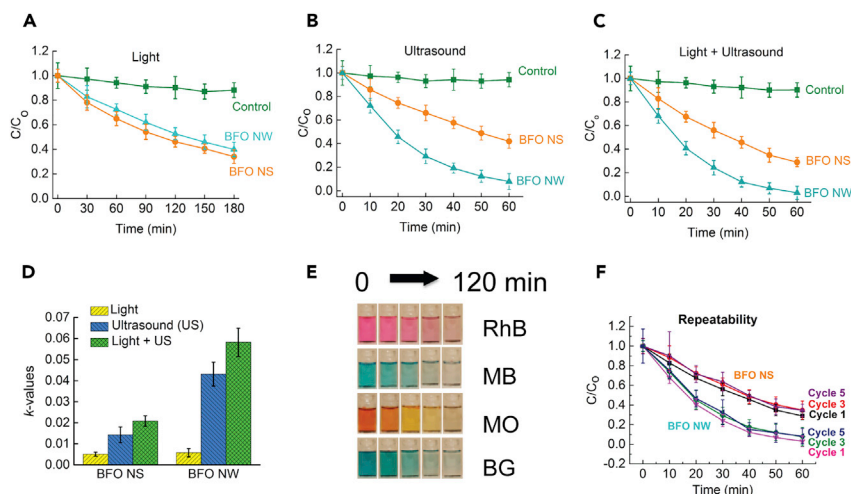
Figure 4. Photo and Piezocatalytic Degradation of RhB Dye Using BFO NSs and NWs

(A) Catalytic degradation curve of RhB using light (n = 5).

(B) Catalytic degradation curve of RhB using ultrasound (n = 5).

(C) Catalytic degradation of RhB using a combination of light and ultrasound stimuli (n = 5).

(D) Comparison of degradation rate constants of RhB obtained for BFO NS and NW under light, ultrasound, and their combination (n = 5).

(E) Visual color change of four different organic dyes in 2 hr under dual stimuli using BFO NWs.

(F) Five consecutive degradation curves obtained for BFO NS and NW under dual stimuli showing a good reusability trend (n = 5).

photocatalytic degradation rate obtained for BFO NS is slightly higher, which can be explained by its lower bandgap value of 2.075 eV in comparison with the NW sample (2.1 eV). Figure 4B presents the piezocatalytic response of BFO samples under ultrasonic wave vibrations. Both BFO samples exhibit a higher RhB degradation rate in comparison with photocatalytic degradation, whereby a 59% and 92% degradation was observed for BFO NS and NW samples in 1 hr, respectively. When the stimuli of light and mechanical vibrations are used simultaneously, the degradation efficiency of the organic dye solution can be further increased to 71% for NSs and 97% for NWs (Figure 4C). A quantitative analysis of these degradation rates is given by comparing their reaction rate constant k, which can be defined by
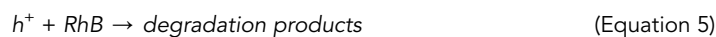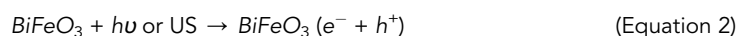
$$k = \ln \frac{C_o}{C} \Big/ t \qquad \text{(Equation 1)}$$

where C_o is the initial RhB concentration and C is the RhB concentration at time t. This calculation is based on the assumption that the kinetics of the RhB degradation reaction catalyzed by the BFO nanostructures are (pseudo)-first-order reactions (Mushtaq et al., 2015, 2016). These results are summarized in Figure 4D, where we can observe that both BFO NS and NW samples display similar photocatalytic rate constants (0.0058 and 0.0051 min^{-1}, respectively). However, under ultrasonic stimulation two interesting phenomena can be observed. First, the RhB degradation rates obtained for both BFO nanostructures are much higher under the piezocatalytic effect than under the photocatalytic effect (2.5 times higher for BFO NS and 8.5 times for BFO NW). Such an enhancement can be explained by the piezotronic effect, which modulates the electrical transporting property at the BFO-electrolyte heterojunction using BFO's internal electric bias. This acts as a driving force for separating the electrons and holes generated by piezocatalysis and, thus, enhances the performance of photochemical reactivity of BFO (Wang et al., 2016; Xue et al., 2015). These surface charges are locally confined, allowing for the chemical reactions to degrade the dye molecules. A second interesting result is that the k-value of BFO NWs (0.0431 min^{-1}) is three times higher than that of the BFO NSs (0.0143 min^{-1}). We assume that, under mechanical stress the high-aspect-ratio BFO NWs experience a greater strain and, hence, a higher strain-induced voltage in comparison with the NS sample. This assumption was verified by using the COMSOL multiphysics software to simulate the induced strain and piezoelectric potential on the surface of a strained

BFO NS and NW (Figure S4). Based on these simulations, we observed that, under similar conditions a higher strain as well as a higher potential was generated on the surface of an NW than on an NS. This assumption was further confirmed by comparing the piezoelectric catalysis performance of BFO NWs with different lengths. With an increasing BFO NW length the corresponding k-values also increased (Figure S5). A similar trend was observed in the case of piezoelectric zinc oxide nanowires, whereby longer nanowires provided higher mechanical to chemical energy conversion efficiency for water splitting using ultrasound (US) (Hong et al., 2010). From Figure 4D, we further observe that when the BFO samples were excited by light and US simultaneously, the observed k-values (k_{dual}) were higher in contrast to when light (k_{light}) or US (k_{us}) were solely used, and even higher than the linear addition of the two, especially for the BFO NWs. This increase in reaction rate offered by piezo-photocatalysis can be explained by an increase in the electron-hole pair formation activity because of a higher energy input available under the dual stimuli. The ability to degrade organic dyes (in the case of BFO NWs) can be greatly enhanced by a factor of 11.4 when a combination of light and mechanical energy is used simultaneously, with a k-value 0.0582 min^{-1} (Table S1 compares the reaction rate constants observed for different materials under light and ultrasonic vibrations). It is worth noting that under dual stimulation, the k-value (k_{dual}) is slightly higher than the linear addition of the respective k-value under only light or US stimulation ($k_{light} + k_{us}$), which indicates that the piezoelectric-driven internal field also helps the photogenerated carriers move to the surface of the BFO nanostructures.

Catalytic efficiency of BFO NWs to successfully harness the dual stimuli and degrade other organic dyes, i.e., methylene blue (MB), methyl orange (MO), and brilliant green (BG), at elevated dye concentrations of 10 mg L^{-1} was also investigated. Figure 4E presents a collage of images taken every 30 min to represent how the BFO NWs were able to degrade all four dyes within 2 hr. These results highlight the ability of BFO nanostructures to successfully scavenge energy from light and waste energy, such as noise or stray vibration, for water remediation (Figure S6). To develop photocatalysts for practical water purification applications, it is essential that they demonstrate not only good efficiency and versatility, but also high stability so that they can be recycled and reused. The reusability of BFO NS and NW samples was examined and is presented in Figure 4F. For both BFO samples we observe a slightly decreasing catalytic performance during the first three consecutive runs. It seems that the following two cycles did not further affect the performance. Long-term analysis will be carried out to examine how the catalytic stability of BFO changes over multiple cycles in future.

To elucidate the possible RhB degradation pathway offered by BFO samples, we first investigated the interaction of the BFO surface with water. According to our DFT calculations, in the presence of a relaxed or strained BFO surface a water molecule can spontaneously dissociate into H^+ and OH^- ions, followed by the highly favored adsorption of OH^- on the BFO surface (see Figure S7). The influence of an external stimulation (such as UV-visible light) leads to the formation of electron-hole pairs inside BFO samples (Figure 5A). Electrons are excited from the valence band (VB) of BFO to the conduction band (CB), leaving behind holes in the VB, and thus creating electron-hole pairs. These electron-hole pairs tend to recombine, leading to a decrease in the number of available charge carriers that can successfully migrate to the surface of BFO and initiate the redox reactions. When US is used to strain BFO, its internal piezoelectric field facilitates the separation of electric charge carriers and their migration toward the surface, thus increasing the probability of initiating the redox reactions. The various steps involved in the degradation of RhB dye by reactive species such as e^-, h^+, $OH^{\cdot}$, and $O_2^{\cdot-}$ are the following:

$$BiFeO_3 + h\upsilon \text{ or US} \rightarrow BiFeO_3 \, (e^- + h^+) \qquad \text{(Equation 2)}$$

$$e^- + O_2 \rightarrow O_2^{-\cdot} \qquad \text{(Equation 3)}$$

$$h^+ + H_2O \rightarrow \cdot OH \qquad \text{(Equation 4)}$$

$$h^+ + RhB \rightarrow degradation \, products \qquad \text{(Equation 5)}$$

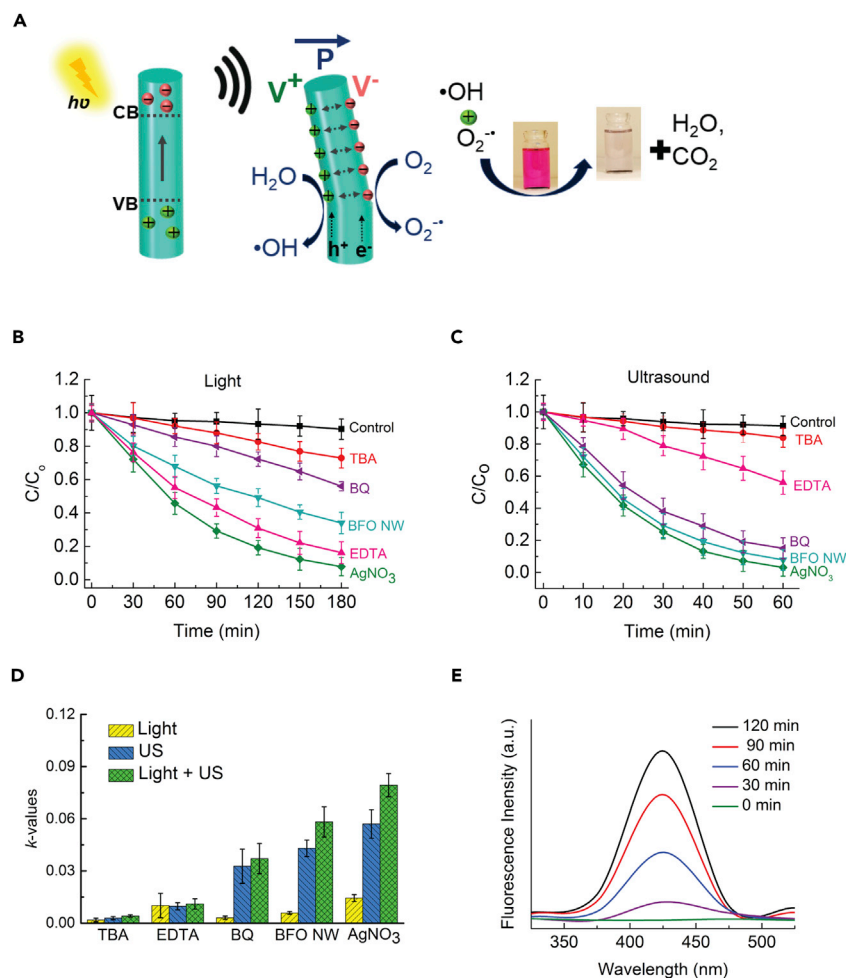$$\cdot OH + RhB \rightarrow degradation \, products \qquad \text{(Equation 6)}$$

Figure 5. The Catalytic Degradation Mechanism of RhB by BFO

(A) Catalytic degradation scheme of BFO NWs under light and ultrasound.

(B) Trapping experiments performed to study catalytic degradation curves obtained for RhB under light (n = 5).

(C) Trapping experiments performed under ultrasound (n = 5).

(D) Comparison of degradation rate constants obtained for different scavengers under light, ultrasound, and their combination (n = 5).

(E) Reaction of terephthalic acid with OH$^{\bullet}$ radicals to produce increasing amounts of fluorescent 2-hydroxyterephthalic acid with peak intensity at 425 nm.

$$O_2^{-\cdot} + RhB \rightarrow degradation\ products \qquad\qquad \text{(Equation 7)}$$

To further determine how these reactive species were involved in the photocatalytic, piezocatalytic, and piezo-photocatalytic reactions, trapping experiments were performed. For this, degradation of RhB dye was carried out in the presence of BFO NWs and different scavengers of the reactive species (Table 1). It can be seen from Figure 5B that the photocatalytic degradation efficiency was increased with the addition of AgNO$_3$ (an electron scavenger) and EDTA (a hole scavenger) (Zhang et al., 2016; Wu et al., 2016), which is probably caused by promoted separation of electron-hole pairs (and thus increased lifetime of electrons/holes) owing to their consumption, or caused by deposition of silver nanoparticles (Mohan et al., 2014). When benzoquinone (BQ) (a superoxide radical O$_2^{-\cdot}$ scavenger) and tert-butyl alcohol (TBA) (a hydroxyl radical OH$^{\bullet}$ scavenger) were added, the photodegradation of RhB decreased. These results reveal that the predominant reactive species for photocatalytic degradation of RhB by BFO NW were the radicals. Trapping experiments were also performed to determine the main reactive species behind the piezocatalytic mechanism (Figure 5C). The addition of AgNO$_3$ (electron scavenger) led to a slightly improved reaction rate, which is probably caused by reasons similar to the ones observed for the photocatalytic experiments (i.e., extended lifetime of holes or

Scavenger	Reactive Species Quenched
AgNO$_3$	e$^-$
EDTA	h$^+$
Tert-butyl alcohol (TBA)	OH$^\bullet$
Benzoquinone (BQ)	O$_2^{\bullet-}$

Table 1. List of All the Scavengers Used in the Trapping Experiments and the Reactive Species They Quench

silver-nanoparticle-enhanced catalytic activity). However, when EDTA (hole scavenger) was added, a strong suppression of RhB degradation was observed, which indicates that holes play an important role in piezocatalytic degradation of RhB. Holes can either directly react with organic dyes to degrade them (Equation 5) or react with water to produce highly reactive OH$^\bullet$ radicals (Equation 4). Hence, their quenching can have a severe impact on RhB degradation. The severe suppression of RhB degradation rate by adding EDTA in the piezocatalytic experiment sharply contrasts with the increase in degradation activity when EDTA was introduced in the photocatalytic experiments. This result can be explained by the different concentration of charge carriers in these two experiments. In the piezocatalytic experiment, the charge carrier's concentration was much higher than that in the photocatalytic experiment, as evidenced by the higher degradation rate. When the holes were trapped, a severe suppression in RhB degradation rate overshadowed any potential degradation rate increase that could have been induced by the prolonged lifetime of electrons. Therefore, in the piezocatalytic experiments the degradation rate decreased compared with the pure BFO NW sample where no scavengers were introduced. However, it should be noted that, since the relative concentration (C/C$_o$) of RhB after 1 hr in both experiments was approximately the same (i.e., about 60% RhB dye was still remaining), the degradation speeds for both photocatalytic and piezocatalytic experiments were the same. This result indicates that the degradation rate for both reactions was determined by the concentration of EDTA used for trapping the holes, which further corroborates our explanation. The trapping of OH$^\bullet$ radicals (that are produced by holes) shows similar trends in both catalytic experiments. The dominating role of holes can be further confirmed by the fact that O$_2^{\bullet-}$ radicals, which are produced by electrons, exhibit a minimal impact on the piezocatalytic RhB degradation. The k-values obtained from the trapping experiments under stimulation of light, US, and the dual stimuli are presented in Figure 5D. For all degradation mechanisms, scavenging either holes or OH$^\bullet$ radicals led to a decrease in the reaction speed, whereas the electrons were the least active species for the degradation of RhB dye. In addition to the trapping experiments, we confirmed the formation of hydroxyl radicals in our degradation experiments by using terephthalic acid as a photoluminescent OH$^\bullet$-trapping agent. Terephthalic acid readily reacts with OH$^\bullet$ radicals to produce a highly fluorescent product, 2-hydroxyterephthalic acid, which emits a unique fluorescent signal at 425 nm (Wu et al., 2016). From the results of this experiment (Figure 5E) we can observe an increase in fluorescence intensity at 425 nm with increasing piezo-photocatalytic reaction time, which offers further proof of OH$^\bullet$ formation during the catalytic reaction.

CONCLUSIONS

In this work, we have successfully fabricated single-crystalline BiFeO$_3$ NSs and NWs that exhibit promising photocatalytic as well as piezocatalytic properties for water remediation. Both BFO nanostructures displayed a slow photocatalytic activity under UV-visible light, with the NS degrading RhB dye to 66% within 3 hr. Under piezocatalytic degradation of RhB, both BFO NSs and NWs were more efficient in degrading RhB, with an elevated efficiency of 59% and 91% within 1 hr, respectively. A comparison between the photocatalytic and piezocatalytic RhB degradation rates revealed that under ultrasonic vibrations, BFO NWs displayed an increase in degradation efficiency up to a factor of 8.5. When piezo-photocatalytic degradation was performed, the degradation efficiency of both BFO NS and NW samples was even higher, with k-values equal to 0.0209 and 0.0582 min^{-1}, respectively. This increase in efficiency under piezoelectric stimulation may be caused by the internal piezoelectric-field-induced bias and its influence on suppressing the electron-hole recombination. Trapping experiments were performed to understand the degradation mechanism behind the photo- and piezocatalytic stimuli using scavengers for the reactive species. Holes and OH$^\bullet$ radicals were demonstrated to be the main reactive species. These results allow for the design of better catalysts that can readily and efficiently harness multiple sources of free energy, such as light and vibration, from their surroundings and use them for environmental applications.

METHODS

All methods can be found in the accompanying Transparent Methods supplemental file.

SUPPLEMENTAL INFORMATION

Supplemental Information includes Transparent Methods, nine figures, and one table and can be found with this article online at https://doi.org/10.1016/j.isci.2018.06.003.

AUTHOR CONTRIBUTIONS

Conceptualization, F.M., B.J.N., and S.P.; methodology, F.M., X.C., M.H.; investigation, F.M., H.T., E.P., J.S., and C.G.; writing: original draft, F.M; writing: review and editing, F.M., X.C., M.H., H.T., E.P., J.S., C.G., B.J.N., and S.P.; supervision X.C., S.P., B.J.N.; funding acquisition, S.P.

DECLARATION OF INTERESTS

The authors declare no competing interests.

REFERENCES

Avinash, B., Yiu-Wing, M., Qian, L., Shing-Chung, W., Yun, L., and Yao, Q.W. (2011). One-dimensional multiferroic bismuth ferrite fibers obtained by electrospinning techniques. Nanotechnology 22, 235702.

Barroso, M., Pendlebury, S.R., Cowan, A.J., and Durrant, J.R. (2013). Charge carrier trapping, recombination and transfer in hematite α-Fe_2O_3 water splitting photoanodes. Chem. Sci. 4, 2724–2734.

Chen, X.-Z., Hoop, M., Shamsudhin, N., Huang, T., Özkale, B., Li, Q., Siringil, E., Mushtaq, F., Di Tizio, L., Nelson, B.J., and Pané, S. (2017). Hybrid magnetoelectric nanowires for nanorobotic applications: fabrication, magnetoelectric coupling, and magnetically assisted in vitro targeted drug delivery. Adv. Mater. 29, 1605458.

Chen, X.-Z., Li, Q., Chen, X., Guo, X., Ge, H.-X., Liu, Y., and Shen, Q.-D. (2013). Nano-imprinted ferroelectric polymer nanodot arrays for high density data storage. Adv. Funct. Mater. 23, 3124–3129.

Chen, X.-Z., Shamsudhin, N., Hoop, M., Pieters, R., Siringil, E., Sakar, M.S., Nelson, B.J., and Pane, S. (2016). Magnetoelectric micromachines with wirelessly controlled navigation and functionality. Mater. Horiz. 3, 113–118.

Chung, K.-T. (1983). The significance of azo-reduction in the mutagenesis and carcinogenesis of azo dyes. Mutat. Res. Rev. Genet. Toxicol. 114, 269–281.

Dong, Y., Dong, W., Liu, C., Chen, Y., and Hua, J. (2007). Photocatalytic decoloration of water-soluble azo dyes by reduction based on bisulfite-mediated borohydride. Catal. Today 126, 456–462.

Ekici, P., Leupold, G., and Parlar, H. (2001). Degradability of selected azo dye metabolites in activated sludge systems. Chemosphere 44, 721–728.

Fracasso, M.E., Leone, R., Brunello, F., Monastra, C., Tezza, F., and Storti, P.V. (1992). Mutagenic activity in wastewater concentrates from dye plants. Mutat. Res. Genet. Toxicol. 298, 91–95.

Harraz, F.A. (2008). Polyethylene glycol-assisted hydrothermal growth of magnetite nanowires: synthesis and magnetic properties. Physica E Low Dimens. Syst. Nanostruct. 40, 3131–3136.

Hong, D., Zang, W., Guo, X., Fu, Y., He, H., Sun, J., Xing, L., Liu, B., and Xue, X. (2016). High piezo-photocatalytic efficiency of CuS/ZnO nanowires using both solar and mechanical energy for degrading organic dye. ACS Appl. Mater. Interfaces 8, 21302–21314.

Hong, K.-S., Xu, H., Konishi, H., and Li, X. (2010). Direct water splitting through vibrating piezoelectric microfibers in water. J. Phys. Chem. Lett. 1, 997–1002.

Jia, Q., Nan, M., and Ya, Y. (2018). Photovoltaic–pyroelectric coupled effect based nanogenerators for self-powered photodetector system. Adv. Mater. Interfaces 5, 1701189.

Julkapli, N., Bagheri, S., and Bee Abd Hamid, S. (2014). Recent advances in heterogeneous photocatalytic decolorization of synthetic dyes. Sci. World J. 2014, 692307.

Jung Min, P., Seiji, N., Masayuki, S., Takeshi, K., and Masanori, O. (2012). Ferroelectric and piezoelectric properties of polycrystalline $BiFeO_3$ thin films prepared by pulsed laser deposition under magnetic field. Jpn. J. Appl. Phys. 51, 09MD05.

Li, H., Sang, Y., Chang, S., Huang, X., Zhang, Y., Yang, R., Jiang, H., Liu, H., and Wang, Z.L. (2015). Enhanced ferroelectric-nanocrystal-based hybrid photocatalysis by ultrasonic-wave-generated piezophototronic effect. Nano Lett. *15*, 2372–2379.

Li, L., Salvador, P.A., and Rohrer, G.S. (2014). Photocatalysts with internal electric fields. Nanoscale *6*, 24–42.

Li, S., Nechache, R., Harnagea, C., Nikolova, L., and Rosei, F. (2012). Single-crystalline $BiFeO_3$ nanowires and their ferroelectric behavior. Appl. Phys. Lett. *101*, 192903.

de Lima, R.O.A., Bazo, A.P., Salvadori, D.M., Rech, C.M., Oliveira, D.D.P., and Umbuzeiro, D.A.G. (2007). Mutagenic and carcinogenic potential of a textile azo dye processing plant effluent that impacts a drinking water source. Mutat. Res. Genet. Toxicol. Environ. Mutagen. *626*, 53–60.

Long, R., and Prezhdo, O.V. (2015). Dopants control electron–hole recombination at perovskite–TiO_2 interfaces: Ab initio time-domain study. ACS Nano *9*, 11143–11155.

Matilainen, A., Vepsäläinen, M., and Sillanpää, M. (2010). Natural organic matter removal by coagulation during drinking water treatment: a review. Adv. Colloid Interface Sci. *159*, 189–197.

Mocherla, P.S.V., Karthik, C., Ubic, R., Rao, M.S.R., and Sudakar, C. (2013). Tunable bandgap in BiFeO3 nanoparticles: the role of microstrain and oxygen defects. Appl. Phys. Lett. *103*, 022910.

Mohan, S., Subramanian, B., and Sarveswaran, G. (2014). A prototypical development of plasmonic multiferroic bismuth ferrite particulate and fiber nanostructures and their remarkable photocatalytic activity under sunlight. J. Mater. Chem. C *2*, 6835–6842.

Mushtaq, F., Asani, A., Hoop, M., Chen, X.-Z., Ahmed, D., Nelson, B.J., and Pané, S. (2016). Highly efficient coaxial TiO_2-PtPd tubular nanomachines for photocatalytic water purification with multiple locomotion strategies. Adv. Funct. Mater. *26*, 6995–7002.

Mushtaq, F., Guerrero, M., Sakar, M.S., Hoop, M., Lindo, A.M., Sort, J., Chen, X., Nelson, B.J., Pellicer, E., and Pane, S. (2015). Magnetically driven Bi_2O_3/BiOCl-based hybrid microrobots for photocatalytic water remediation. J. Mater. Chem. A *3*, 23670–23676.

Nan, M., Kewei, Z., and Ya, Y. (2017). Photovoltaic–pyroelectric coupled effect induced electricity for self-powered photodetector system. Adv. Mater. *29*, 1703694.

Núñez, O., Rivas, C., and Vargas, R. (2017). Minimizing electron-hole recombination in modified TiO_2 photocatalysis: electron transfer to

solution as rate-limiting step in organic compounds degradation. J. Phys. Org. Chem. *30*, 3659.

Pesci, F.M., Wang, G., Klug, D.R., Li, Y., and Cowan, A.J. (2013). Efficient suppression of electron–hole recombination in oxygen-deficient hydrogen-treated TiO_2 nanowires for photoelectrochemical water splitting. J. Phys. Chem. C *117*, 25837–25844.

Qi, J., Ma, N., Ma, X., Adelung, R., and Yang, Y. (2018). Enhanced photocurrent in BiFeO3 materials by coupling temperature and thermo-phototronic effects for self-powered ultraviolet photodetector system. ACS Appl. Mater. Interfaces *10*, 13712–13719.

Sakthivel, S., Shankar, M.V., Palanichamy, M., Arabindoo, B., Bahnemann, D.W., and Murugesan, V. (2004). Enhancement of photocatalytic activity by metal deposition: characterisation and photonic efficiency of Pt, Au and Pd deposited on TiO_2 catalyst. Water Res. *38*, 3001–3008.

Singh, S., and Khare, N. (2017). Coupling of piezoelectric, semiconducting and photoexcitation properties in $NaNbO_3$ nanostructures for controlling electrical transport: realizing an efficient piezo-photoanode and piezo-photocatalyst. Nano Energy *38*, 335–341.

Singh, S.K., Ishiwara, H., and Maruyama, K. (2006). Room temperature ferroelectric properties of Mn-substituted $BiFeO_3$ thin films deposited on Pt electrodes using chemical solution deposition. Appl. Phys. Lett. *88*, 262908.

Soltani, T., and Entezari, M.H. (2013). Sono-synthesis of bismuth ferrite nanoparticles with high photocatalytic activity in degradation of Rhodamine B under solar light irradiation. Chem. Eng. J. *223*, 145–154.

Song, C.Y., Xu, J., Yimamu, A., and Wang, L. (2014). Hydrothermal synthesis of perovskite bismuth ferrite micro/nano powders. Integr. Ferroelectr. *153*, 33–41.

Sun, B., Han, P., Zhao, W., Liu, Y., and Chen, P. (2014). White-light-controlled magnetic and ferroelectric properties in multiferroic $BiFeO_3$ square nanosheets. J. Phys. Chem. C *118*, 18814–18819.

Umbuzeiro, G.D.A., Freeman, H.S., Warren, S.H., Oliveira, D.P.D., Terao, Y., Watanabe, T., and Claxton, L.D. (2005). The contribution of azo dyes to the mutagenic activity of the Cristais River. Chemosphere *60*, 55–64.

Wang, L., Liu, S., Wang, Z., Zhou, Y., Qin, Y., and Wang, Z.L. (2016). Piezotronic effect enhanced photocatalysis in strained anisotropic ZnO/tio2 nanoplatelets via thermal stress. ACS Nano *10*, 2636–2643.

Wu, J., Mao, W., Wu, Z., Xu, X., You, H., Xue, A.X., and Jia, Y. (2016). Strong pyro-catalysis of pyroelectric $BiFeO_3$ nanoparticles under a room-temperature cold-hot alternation. Nanoscale *8*, 7343–7350.

Xian, T., Yang, H., Dai, J.F., Wei, Z.Q., Ma, J.Y., and Feng, W.J. (2011). Photocatalytic properties of $BiFeO_3$ nanoparticles with different sizes. Mater. Lett. *65*, 1573–1575.

Xiao, G., Yongming, F., Deyi, H., Binwei, Y., Haoxuan, H., Qiang, W., Lili, X., and Xinyu, X. (2016). High-efficiency sono-solar-induced degradation of organic dye by the piezophototronic/photocatalytic coupling effect of FeS/ZnO nanoarrays. Nanotechnology *27*, 375704.

Xie, S.H., Li, J.Y., Proksch, R., Liu, Y.M., Zhou, Y.C., Liu, Y.Y., Ou, Y., Lan, L.N., and Qiao, Y. (2008). Nanocrystalline multiferroic $BiFeO_3$ ultrafine fibers by sol-gel based electrospinning. Appl. Phys. Lett. *93*, 222904.

Xu, X., Xu, Q., Huang, Y., Hu, X., Huang, Y., Wang, G., Hu, X., and Zhuang, N. (2016). Control of crystal phase and morphology in hydrothermal synthesis of $BiFeO_3$ crystal. J. Cryst. Growth *437*, 42–48.

Xue, X., Zang, W., Deng, P., Wang, Q., Xing, L., Zhang, Y., and Wang, Z.L. (2015). Piezo-potential enhanced photocatalytic degradation of organic dye using ZnO nanowires. Nano Energy *13*, 414–422.

Yan, H., Wang, X., Yao, M., and Yao, X. (2013). Band structure design of semiconductors for enhanced photocatalytic activity: the case of TiO_2. Prog. Mater. Sci. Mater. Inter. *23*, 402–407.

Yang, X., Xu, G., Ren, Z., Wei, X., Chao, C., Gong, S., Shen, G., and Han, G. (2014). The hydrothermal synthesis and formation mechanism of single-crystalline perovskite $BiFeO_3$ microplates with dominant (012) facets. CrystEngComm *16*, 4176–4182.

Yun, J., Kewei, Z., and Ya, Y. (2018). A one-structure-based multieffects coupled nanogenerator for simultaneously scavenging thermal, solar, and mechanical energies. Adv. Sci. *5*, 1700622.

Zhang, N., Chen, D., Niu, F., Wang, S., Qin, L., and Huang, Y. (2016). Enhanced visible light photocatalytic activity of Gd-doped $BiFeO_3$ nanoparticles and mechanism insight. Sci. Rep. *6*, 26467.

Zhang, N., Liu, S., Fu, X., and Xu, Y.-J. (2011). Synthesis of $M@TiO_2$ (M = Au, Pd, Pt) core–shell nanocomposites with tunable photoreactivity. J. Phys. Chem. C *115*, 9136–9145.

Supplemental Information

Piezoelectrically Enhanced Photocatalysis

with BiFeO$_3$ Nanostructures

for Efficient Water Remediation

Fajer Mushtaq, Xiangzhong Chen, Marcus Hoop, Harun Torlakcik, Eva Pellicer, Jordi Sort, Chiara Gattinoni, Bradley J. Nelson, and Salvador Pané

TRANSPARENT METHODS

Fabrication of BiFeO₃ nanostructures BiFeO$_3$ (BFO) nanosheets (NS) and nanowires (NW) were fabricated by a tunable hydrothermal synthesis approach. For the fabrication of BFO NS, Bi(NO$_3$)·5H$_2$O and FeCl$_3$·6H$_2$O were dissolved in a stoichiometric 1:1 molar ratio in acetone using continuous mechanical stirring and ultrasound. Next, DI water was added followed by concentrated ammonia under vigorous stirring to adjust the pH to 11. The resulting sediment was centrifuged, washed several times with DI water to reach a neutral pH value, and dissolved in 40 mL of DI water. NaOH (5 M) was added to the above solution and stirred for 1 h at room temperature. Finally, the above solution was transferred to a 50 mL sealed, Teflon-lined steel autoclave and heated at 140 ˚C for 72 h. The black powder obtained was washed with DI water and ethanol and dried at 60 ˚C for characterization.

For the fabrication of BFO NW, the same fabrication procedure was followed until the addition of 5 M NaOH. After this step, 5 mL of polyethylene glycol (Mn 400) was added to the 40 mL solution at 60 ˚C and stirred for 30 min. Finally, this solution was transferred to a 50 mL capacity sealed, Teflon-lined steel autoclaved and heated at 180 ˚C for 72 h. BFO NWs with different lengths were prepared by varying reaction times (details are provided in Figure S5).

Material characterization The morphology of the resulting BFO nanostructures was investigated by scanning electron microscopy (SEM, Zeiss ULTRA 55, Zeiss, Oberkochen, Germany), transmission electron microscopy (TEM, FEI F30, FEI Co., Hillsboro, OR), and scanning transmission electron microscopy (STEM, FEI F30). The crystallographic structure of the nanostructures was analyzed by X-ray diffraction on a Bruker AXS D8 Advance X-ray diffractometer, equipped with a Cu target with a wavelength of 1.542 Å. Cell parameters, crystallite sizes and microstrains were evaluated by Rietveld refinement using the Materials Analysis Using Diffraction (MAUD) software (overlapped experimental and computed patterns for both BFO NSs and NWS are provides in Figure S8).(Lutterotti et al., 1990) The local crystallographic structure was studied by selected area electron diffraction (SAED). Piezoresponse force microscopy (PFM) investigations were performed on a commercial atomic force microscope (NT-MDT Ntegra Prima). Pt-coated Si probes, i.e. HA-FM01/Pt, were used, and the imaging contact force set-points were carefully controlled. To perform PFM measurements on the long BFO NW, the nanowires were fixed by depositing carbon bands on their two ends using focused ion beam (FIB) (Figure S9). For domain imaging, AC signals (amplitude $V_{AC} = 1$ V) were used to excite the surface oscillations. To acquire local piezoresponse loops, ac signals ($V_{AC} = 0.5$ V) were superimposed on triangular staircase wave with DC switching from -10 V to 10 V. UV-Vis diffuse reflectance spectra (DRS) was acquired by a Cary 4000 UV-vis spectrophotometer. $BaSO_4$ was used as the reflectance standard.

Catalytic performance measurement Catalytic experiments were performed to study the degradation of RhB dye in the presence of our BFO structures. An RhB concentration of 4 mg L^{-1} was chosen to perform degradation experiments and 30 mg of BFO NSs and NWs were dispersed

in 30 mL of RhB solution under continuous agitation and the adsorption-desorption equilibrium was allowed to reach before starting the experiment. The reaction temperature was maintained at 25 ± 2 °C to negate the effect of temperature. For the photocatalytic experiments, the samples were irradiated with UV-visible light (300 nm $< \lambda <$ 600 nm) using a 300 W Xenon lamp (Asahi Spectra, MAX-303). For the piezo-catalytic measurements, samples were subjected to stress using an ultrasonic source (VWR USC300DF, nominal power and frequency: 80 W, 132 kHz) and kept in a dark environment (to avoid photocatalytic degradation). For the piezo-photocatalytic degradation experiments, the above mentioned light source was used in combination with the ultrasonic source. A UV-Vis spectrophotometer (Tecan Infinite 200 Pro) was used to obtain the fluorescent spectra of RhB over time by taking aliquots of irradiated RhB solution.

Trapping experiments To investigate the degradation pathways behind photocatalytic and piezocatalytic mechanism, we performed trapping experiments using different scavengers. $AgNO_3$ (2 mM), ethylene diamine tetraacetic acid (EDTA, 2 mM), tert-butyl alcohol (TBA, 2 mM) and benzoquinone (BQ, 0.5 mM) solutions were prepared in a 4 mg L^{-1} RhB solution. Next, experiments for photocatalysis, piezocatalysis and piezo-photocatalysis were performed in a similar manner as discussed above. For the experiment to probe the formation of OH$^•$ radicals, 0.5 mM terephthalic acid solution was prepared in 30 mL DI water with 30 mg of BFO NWs and subjected to piezo-photocatalysis, after which the solution's intensity was monitored at 425 nm every 30 mins.
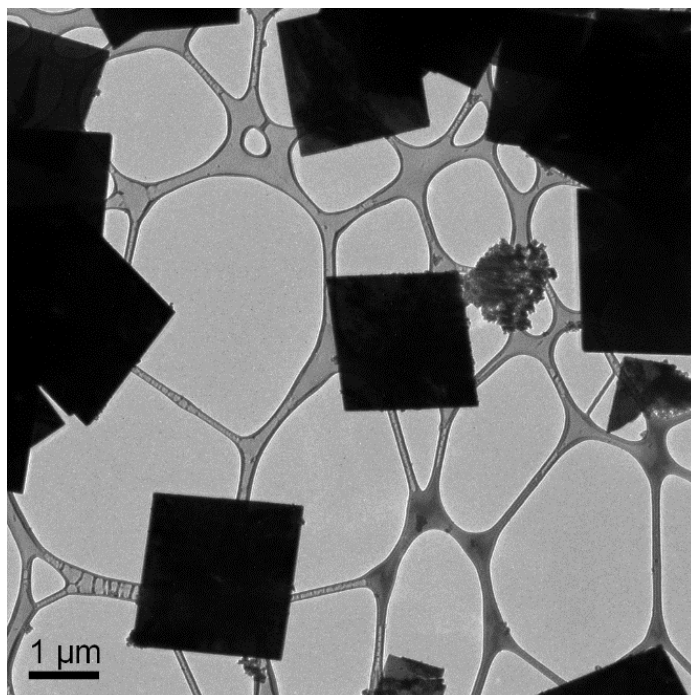
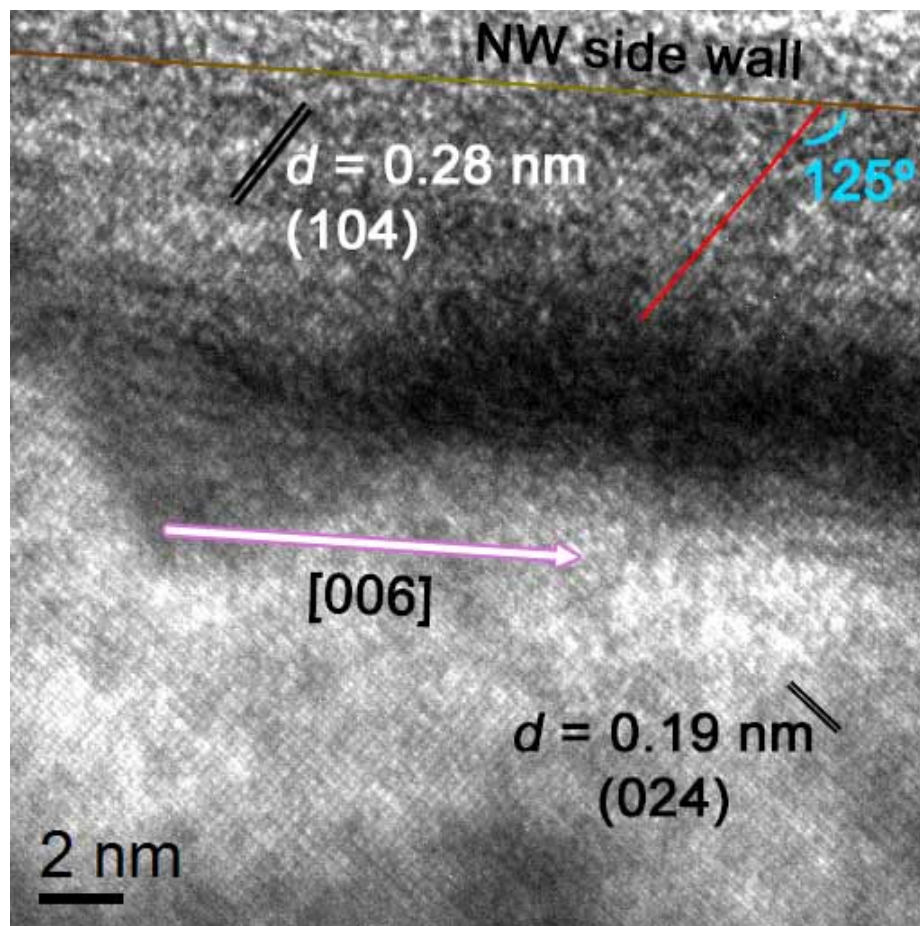**Figure S1: TEM image showing a few BFO NS, related to Figure 1.**

Figure S2: HRTEM image taken at the edge of a BFO NW showing its growth direction along the [006] axis, related to Figure 2.
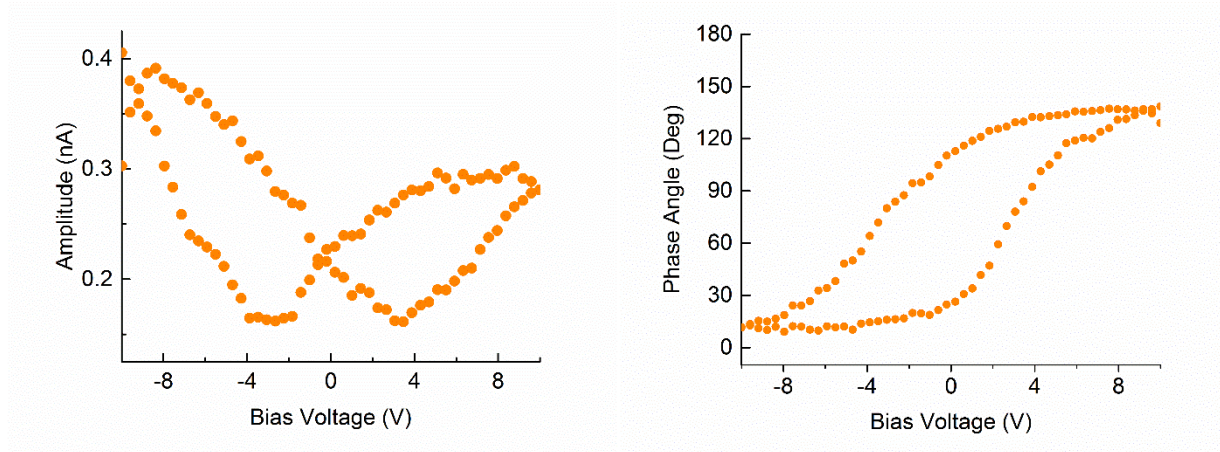
Figure S3: PFM analysis performed on a BFO NS, related to Figure 3.

Amplitude (left) and phase (right) loops obtained for a single BFO NS using PFM.

Multiphysics simulation and comparison of piezoelectric performance of BFO NS and NW

The theoretical piezo-electic performance of the BFO NS and NW in the degradation experiments was also investitaged in a multiphysics simulataion. The ultrasonic source (VWR USC300DF, nominal power and frequency: 80 W, 132 kHz) generates pressure waves with amplitudes up to 6.7 kPa calculated from reference. This pressure can induce compressive, tensile or shear stress in the multiferroic BFO structures.(Dai et al., 2017) The simulated BFO NS was implemented as a symmetric cuboid with a thickness of 145 nm and an edge length of 2.27 um, and BFO NW was implemented as a column with a thickness of 650 nm and a total length of 32 um (Young´s modulus of 189 GPa with a Poisson´s ratio of 0.35).(Aimon et al., 2012) The piezoelectric characteristics of this material with R3c symmetry is described by the piezo-electric coupling matrix

$$d = \begin{bmatrix} 13.5 & 0 & 0 & 0 & 9 & 0 \\ 0 & 13.5 & 0 & 9 & 0 & 0 \\ 3 & 3 & 50 & 0 & 0 & 0 \end{bmatrix} \cdot 10^{-12} [C/N]$$

and the compliance matrix

$$s_E = \begin{bmatrix} 0.0182167 & -0.0006753 & -0.0179691 & 0.0011707 & 0 & 0 \\ \cdot & 0.0182167 & -0.0179691 & -0.0011707 & 0 & 0 \\ \cdot & \cdot & 0.0492076 & 0 & 0 & 0 \\ \cdot & \cdot & \cdot & 0.0192123 & 0 & 0 \\ \cdot & \cdot & \cdot & \cdot & 0.0192123 & 2 \cdot 0.0011707 \\ \cdot & \cdot & \cdot & \cdot & \cdot & 0.0377839 \end{bmatrix} \cdot 10^{-9}[1/Pa]$$

which were determined from literature.(Graf et al., 2015, Nye, 2009, Aimon et al., 2012, Wang et al., 2009) As the material is not isotropic, the preferred growth directions of [024] for the BFO NS and [006] for the BFO NW had to be taken into account. The mechanical and electrical boundary conditions were set on the back face of the BFO NS and the bottom face of the BFO NW. Since the geometric shape of both BFO structures have several symmetries, multiple ways of applying stress on to the suface exist such as the compressive, tensile and shear. Here, we present the most pronounced combinations for each structure. On the basis of the results obtained, we can conclude that for both BFO NS and BFO NW, an application of a shear stress results in the highest generated surface potential, where a force per unit area of 6.7 kPa is simultaneously applied on the top surface of the structures along the positive x-axis and on the front left surface along the negative z-axis (Figure S4 f,l). In every scenario, BFO NW expereinces higher induced potentials than the NS sample. This suggests that the shape of the BFO structure can influnce its piezo-electric performance, which is also supported by the results obtained from the degradation experiments.
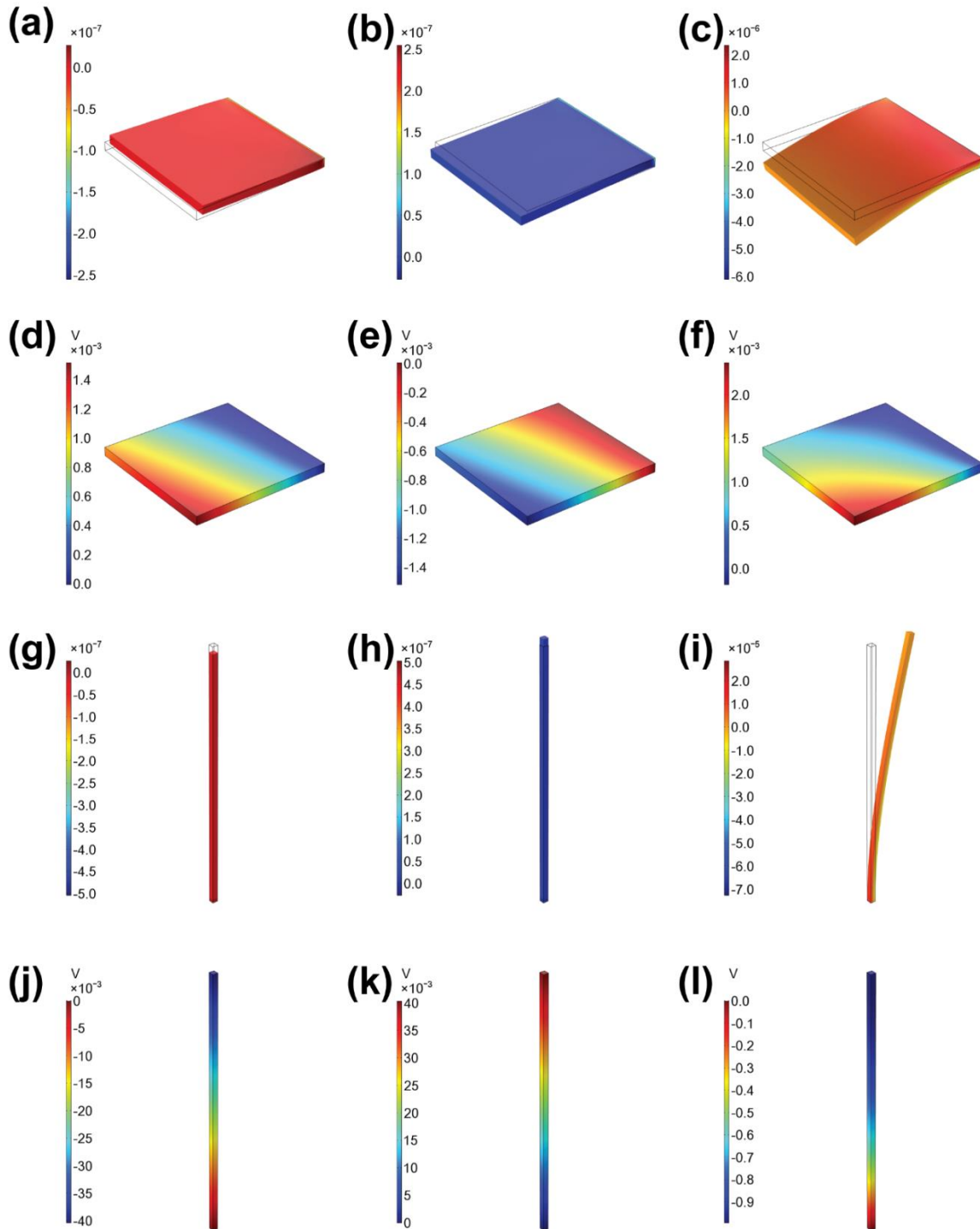
Figure S4: COMSOL multiphysics simulations obtained for BFO NS and NW showing different deformations, related to Figure 4.

(a) under compressive, (b) tensile and (c) shear stress with the correspondingly induced piezoelectric potential (d-f). Similarly, for BFO NW, the strain under (g) compressive, (h) tensile, and (i) shear stress and the correspondingly induced piezoelectric potential (j-l) are also presented.
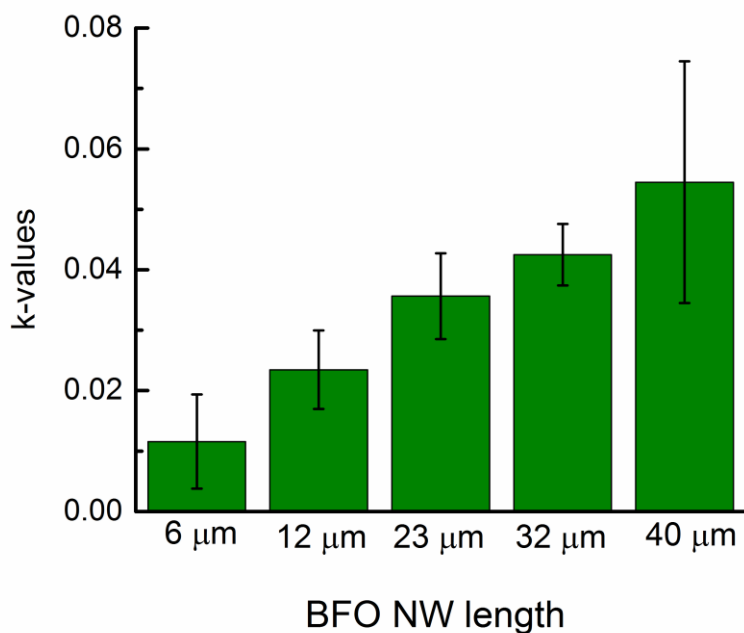
Figure S5: RhB degradation rate constant values obtained under piezo-catalysis for BFO NW with increasing lengths, related to Figure 4.

The different lengths were prepared by varying reaction times i.e. 12 hr (6 µm), 24 hr (12 µm), 48 hr (23 µm), 72 hr (32 µm) and 80 hr (40 µm).

Architecture/Composition	Energy source	k-value (min^{-1})	Ref.
Coaxial TiO$_2$-PtPd NWs	Light: 450 W, Xe lamp $\lambda > 420$ nm	0.071	(Mushtaq et al., 2016)
Metal- TiO$_2$ core-shell NPs	Light: 300 W, Xe lamp $\lambda > 400$ nm	0.013 (TiO$_2$-Au) 0.038 (TiO$_2$-Pd) 0.016 (TiO$_2$-Pt)	(Zhang et al., 2011)
Polyaniline (PANI)/TiO$_2$ nanocomposite	Light: 100 W, W-halogen lamp, $\lambda > 400$ nm	0.052 (PANI-TiO$_2$) 0.0035 (TiO$_2$)	(Masid et al., 2015)
Nanopowders of novel photocatalysts	Light: 500 W, Xe lamp 400 nm $< \lambda <$ 800 nm	0.019 (ZnBiSbO$_4$) 0.004 (N-TiO$_2$) 0.005 (CdBiYO$_4$)	(Luan et al., 2014)
MWCNT/TiO$_2$ composite	Light: 500 W, halogen lamp, $\lambda > 400$ nm	0.0036 (TiO$_2$) 0.0149 (MWCNT-TiO$_2$)	(Abdullahi et al., 2015)
TiO$_2$/CuS Core/Shell nanowires	Light: 500 W, Xe lamp $\lambda > 420$ nm	0.0019 (TiO$_2$) 0.014 (CuS NPs on TiO$_2$) 0.036 (Core-shell TiO$_2$-CuS)	(Khanchandani et al., 2016)
FeS/ZnO nanowire array	Light: 500 W, Xe lamp US: 200 W	2.5 (100 mg loading)	(Xiao et al., 2016)
CuS/ZnO nanowire array	Light: 500 W, Xe lamp 200 nm $< \lambda <$ 1100 nm US: 200 W	4 (100 mg loading)	(Hong et al., 2016)
Single-phase BiFeO$_3$ nanostructures	Light: 450 W, Xe lamp US: 80 W	0.06	This work

Table S1 Comparison of rate constants obtained for various catalysts under visible light and ultrasonic vibrations. Related to Figure 4
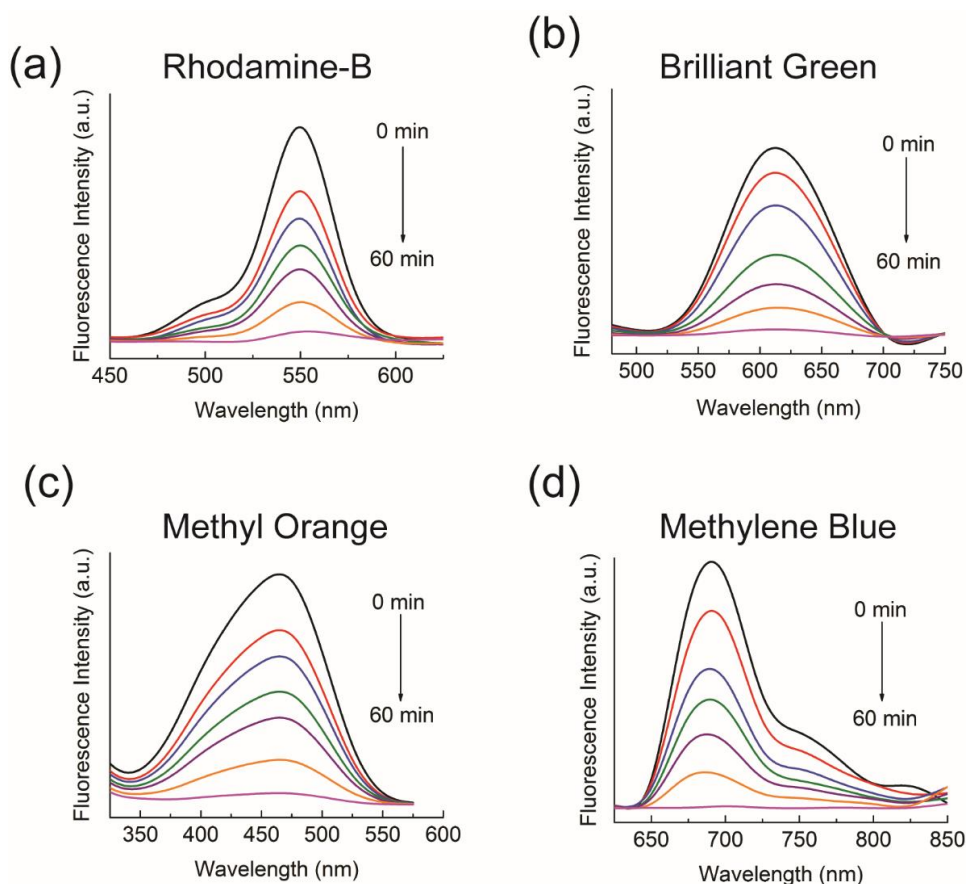
Figure S6: Piezo-photocatalytic degradation of four different organic dyes using BFO NWs under stimulation for 1 h, related to Figure 4.

DFT calculation on water adsorption on BiO-terminated (100) surface

Density functional theory (DFT) calculations were performed with VASP.(Kresse et al., 1993, Kresse et al., 1996a, Kresse et al., 1996b) The inner core electrons were replaced by projected atomic waves(Kresse et al., 1999) and the optB86b-vdW functional(Jiří et al., 2010) was used. OptB86b-vdW is a non-local functional which accounts for long-range van der Waals interaction and it is part of the vdW-DF family of functionals(Dion et al., 2004) which have been shown to perform well for the adsorption of water and other small molecules, especially on metals(Klimeš et al., 2012, Gattinoni et al., 2015, Liriano et al., 2017, Carrasco et al., 2011, Carrasco et al., 2014). A plane wave cutoff of 500eV and a 5x5x5 Mokhorst-Pack k-points mesh was used. On-site Coulomb interaction in the Fe d orbitals were taken into account by the addition of a Hubbard U, in the Dudarev approach(Liriano et al., 2017) with a U-J=4 eV. This setup led to a good description of bulk BFO with the lattice constant a, and rhombohedral angle α being within 1% of the experimental values (measured values for a and α are 3.975 and 59.59, while the experimental

values are 3.983 and 59.35, respectively). The magnetic moment, μ values were within 10% of the experimental values, with the measured value being 4.10 and the experimental value being 3.75. The value of the band gap, 2.25 eV, is within the experimentally measured range (1.3-3.0)(Higuchi et al., 2008, Reda et al., 2012) and close to the band gap in the nanocrystals presented in this paper.

A slab geometry with a (001) surface normal and a 2x2 area is employed. We introduce ~15 Å of vacuum between periodic images of the slab in the z direction. The k-points mesh in the slabs is 2x2x1. The convergence criterion on the forces is 5x 10^{-3} eV/ Å. The bottom to layers of the slab are fixed to bulk position while the atoms in the upmost layers are allowed to relax. Seven-layer-thick slabs were sufficient to converge the cleavage energy ($E_{cl}=E_{BiO}-E_{FeO2}-nxE_{bulk}$) within 10 meV and were thus employed in all calculations. The adsorption energies were calculated as: $E_{ads}=E_{whole}-E_{slab}-E_{H2O}$, where E_{whole}, E_{slab} and E_{H2O} are the total energies of, respectively, the whole adsorbed system, the substrate and the water molecule in the gas phase.

Two surface terminations are possible, a BiO and a FeO_2 termination. We have focused on the BiO-terminated surface. Two polarization direction are possible, up and down. A drive for the dissociation of water was defined as a more negative adsorption energy of a co-adsorbed OH and H rather than for an intact H_2O.

A propensity for dissociation was observed for the up-polarized surface, where the adsorption energy for the intact molecule is $E_{ads}=-2.98$ eV and for the dissociated one is $E_{ads}=-3.03$ eV. This holds true for a range of strains of the substrate, between -5% and +5%.

In the case of the down-polarized surface, a drive for dissociation was not observed, the adsorption energy of the intact molecule being $E_{ads}=-3.01$ eV and for the dissociated molecule $E_{ads}=-2.36$ eV.

In all cases the most stable adsorption configuration was found to be, for the intact (dissociated) structure, with the H_2O (OH) sitting in the bridge position between two Bi atoms with on H atom pointing towards (adsorbed to) the neighboring O atom (as shown in Fig. S7).
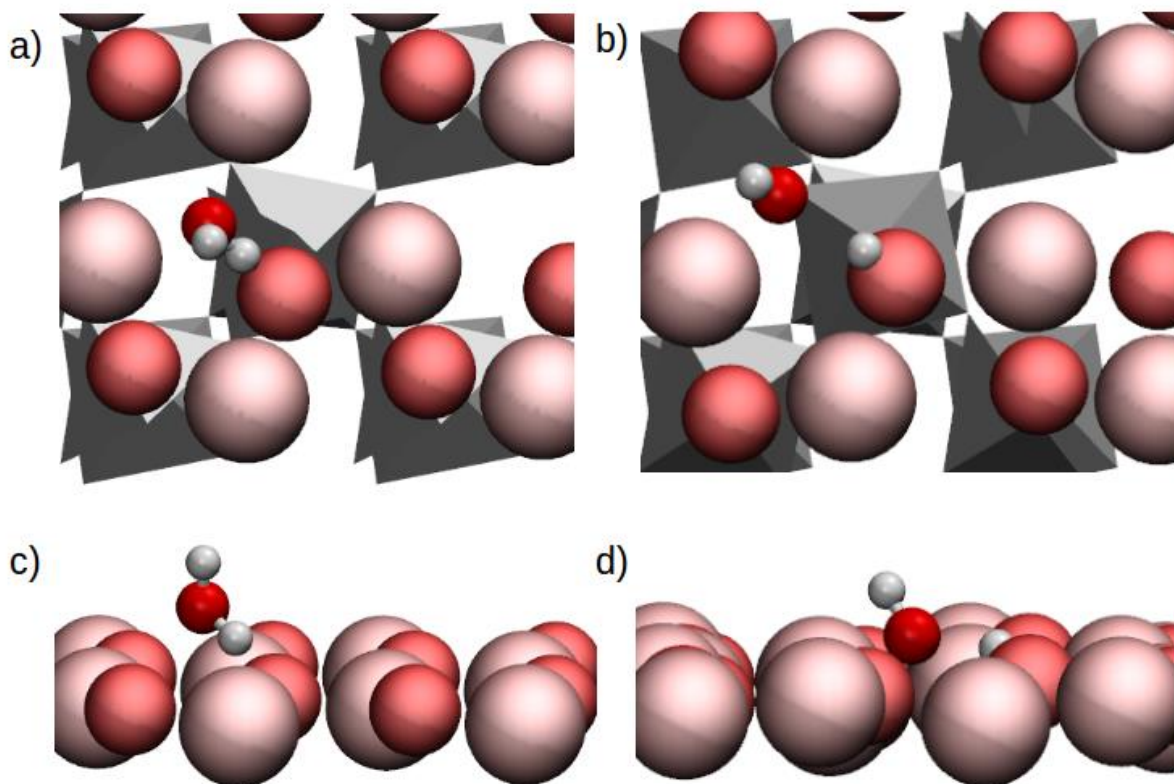
Figure S7: Adsorption structure of intact and dissociated water on the BiO-terminated (100) BFO surface. Both up and down polarized surfaces present the same adsorption structure, related to Figure 5.

(a) Top and (c) side view of a single H_2O adsorbed in the Bi-Bi bridge position.

(b) Top and (d) side view of a dissociated HO+H. O is in red, H in white and Bi in pink. Only the top layer atoms of BFO are shown, the other layers are only shown with the grey oxygen octahedral.
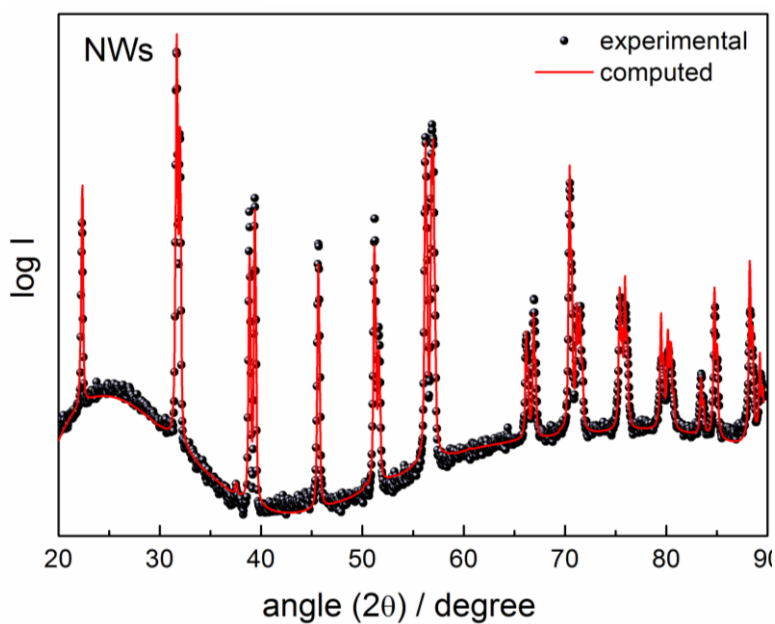
(a)
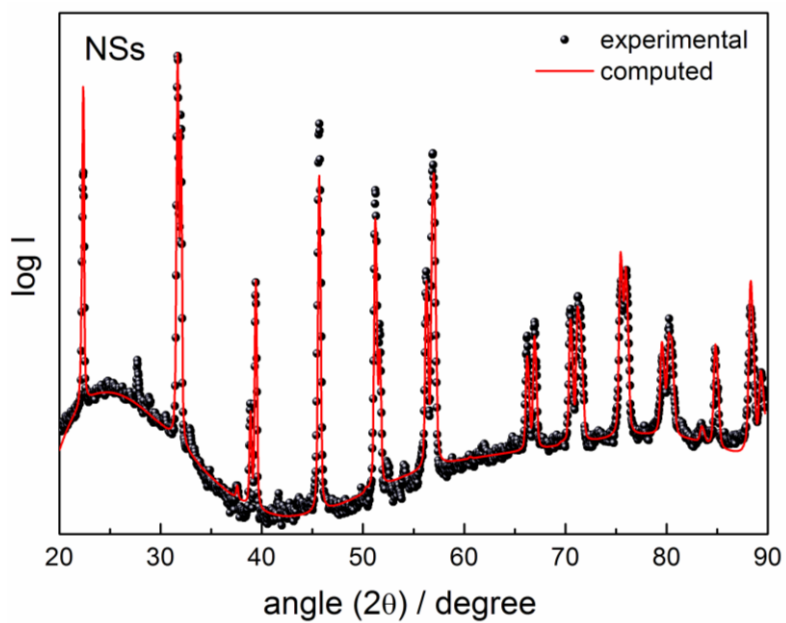
(b)

Figure S8: Rietveld analysis performed by MAUD software with overlapped experimental and computed XRD pattern, related to Figure 2.
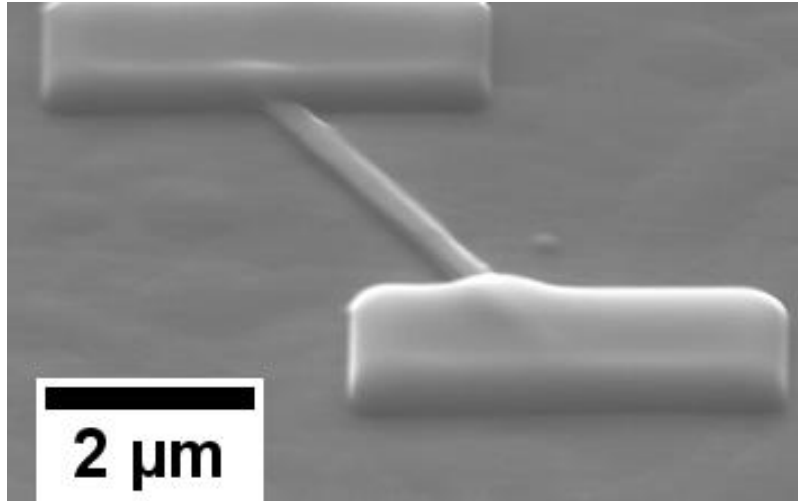
(a) BFO NSs. (b) BFO NWs.

Figure S9: An SEM image showing a BFO NW fixed by carbon bands deposited using FIB, related to Figure 3.

SUPPLEMENTAL REFERENCES

Abdullahi, N., Saion, E., Shaari, A. H., Al-Hada, N. M. and Keiteb, A. (2015). Optimisation of the Photonic Efficiency of TiO_2 Decorated on MWCNTs for Methylene Blue Photodegradation. PLoS ONE 10, 125511.

Aimon, N. M., Liao, J. and Ross, C. A. (2012). Simulation of inhomogeneous magnetoelastic anisotropy in ferroelectric/ferromagnetic nanocomposites. App. Phys. Lett. 101, 232901.

Carrasco, J., Liu, W., Michaelides, A. and Tkatchenko, A. (2014). Insight into the description of van der Waals forces for benzene adsorption on transition metal (111) surfaces. J. Chem. Phys. 140, 084704.

Carrasco, J., Santra, B., Klimeš, J. and Michaelides, A. (2011). To Wet or Not to Wet? Dispersion Forces Tip the Balance for Water Ice on Metals. Phys. Rev. Lett. 106, 026101.

Dai, B., Lu, C., Kou, J., Xu, Z. and Wang, F. (2017). Photocatalytic performance of PMN-PT@TiO_2 highly enhanced by alternative spatial electric field induced charge separation effect. J. Alloys Compd. 696, 988-995.

Dion, M., Rydberg, H., Schröder, E., Langreth, D. C. and Lundqvist, B. I. (2004). Van der Waals Density Functional for General Geometries. Phy. Rev. Lett. 92, 246401.

Gattinoni, C. and Michaelides, A. (2015). Understanding corrosion inhibition with van der Waals DFT methods: the case of benzotriazole. Faraday Discuss. 180, 439-458.

Graf, M., Sepliarsky, M., Machado, R. and Stachiotti, M. G. (2015). Dielectric and piezoelectric properties of $BiFeO_3$ from molecular dynamics simulations. Solid State Commun. 218, 10-13.

Higuchi, T., Liu, Y.-S., Yao, P., Glans, P.-A., Guo, J., Chang, C., Wu, Z., Sakamoto, W., Itoh, N., Shimura, T., Yogo, T. and Hattori, T. (2008). Electronic structure of multiferroic $BiFeO_3$ by resonant soft x-ray emission spectroscopy. Phys. Rev. B 78, 085106.

Hong, D., Zang, W., Guo, X., Fu, Y., He, H., Sun, J., Xing, L., Liu, B. and Xue, X. (2016). High Piezo-photocatalytic Efficiency of CuS/ZnO Nanowires Using Both Solar and Mechanical Energy for Degrading Organic Dye. ACS Appl. Mater. Inter. 8, 21302-21314.

Jiří, K., David, R. B. and Angelos, M. (2010). Chemical accuracy for the van der Waals density functional. J. Phys. Condens. Matter. 22, 022201.

Khanchandani, S., Kumar, S. and Ganguli, A. K. (2016). Comparative Study of TiO_2/CuS Core/Shell and Composite Nanostructures for Efficient Visible Light Photocatalysis. ACS Sustain. Chem. Eng. 4, 1487-1499.

Klimeš, J. and Michaelides, A. (2012). Perspective: Advances and challenges in treating van der Waals dispersion forces in density functional theory. J. Chem. Phys. 137, 120901.

Kresse, G. and Furthmüller, J. (1996a). Efficiency of ab-initio total energy calculations for metals and semiconductors using a plane-wave basis set. Comput. Mater. Sci. 6, 15-50.

Kresse, G. and Furthmüller, J. (1996b). Efficient iterative schemes for ab initio total-energy calculations using a plane-wave basis set. Phys. Rev. B 54, 11169-11186.

Kresse, G. and Hafner, J. (1993). Ab initio molecular dynamics for liquid metals. Phys. Rev. B 47, 558-561.

Kresse, G. and Joubert, D. (1999). From ultrasoft pseudopotentials to the projector augmented-wave method. Phys. Rev. B 59, 1758-1775.

Liriano, M. L., Gattinoni, C., Lewis, E. A., Murphy, C. J., Sykes, E. C. H. and Michaelides, A. (2017). Water–Ice Analogues of Polycyclic Aromatic Hydrocarbons: Water Nanoclusters on Cu(111). J. Am. Chem. Soc. 139, 6403-6410.

Luan, J., Chen, M. and Hu, W. (2014). Synthesis, Characterization and Photocatalytic Activity of New Photocatalyst $ZnBiSbO_4$ under Visible Light Irradiation. Int. J. Mol. Sci. 15, 9459-9480.

Lutterotti, L. and Scardi, P. (1990). Simultaneous structure and size–strain refinement by the Rietveld method. J. App. Cryst. 23, 246-252.

Masid, S., Tayade, R. and Rao, N. N. (2015). Efficient visible light active Polyaniline/TiO_2 nanocomposite photocatalyst for degradation of Reactive Blue 4. Inter. J. Photocatal. Photon 119, 190-203.

Mushtaq, F., Asani, A., Hoop, M., Chen, X.-Z., Ahmed, D., Nelson, B. J. and Pané, S. (2016). Highly Efficient Coaxial TiO_2-PtPd Tubular Nanomachines for Photocatalytic Water Purification with Multiple Locomotion Strategies. Adv. Funct. Mater. 26, 6995-7002.

Nye, J. F. 2009. *Physical properties of crystals : their representation by tensors and matrices*, Oxford : Clarendon Press.

Reda, M., Guy, S., Olivier, R., Dorothée, C. and Michel, V. (2012). Photoluminescence Investigation of Defects and Optical Band Gap in Multiferroic $BiFeO_3$ Single Crystals. Appl. Phys. Express 5, 035802.

Wang, Y. L., Wu, Z. H., Deng, Z. C., Chu, L. Z., Liu, B. T., Liang, W. H. and Fu, G. S. (2009). First-Principle Calculation of Elastic Compliance Coefficients for $BiFeO_3$. Ferroelectrics 386, 133-138.

Xiao, G., Yongming, F., Deyi, H., Binwei, Y., Haoxuan, H., Qiang, W., Lili, X. and Xinyu, X. (2016). High-efficiency sono-solar-induced degradation of organic dye by the piezophototronic/photocatalytic coupling effect of FeS/ZnO nanoarrays. Nanotechnology 27, 375704.

Zhang, N., Liu, S., Fu, X. and Xu, Y.-J. (2011). Synthesis of $M@TiO_2$ (M = Au, Pd, Pt) Core–Shell Nanocomposites with Tunable Photoreactivity. J. Phys. Chem. C 115, 9136-9145.